AGU PUBLICATIONS

JGR

Journal of Geophysical Research: Atmospheres

RESEARCH ARTICLE
10.1002/2013JD021265

Key Points:
- Moist processes are key in intrinsic error growth of tropical cyclones
- Cascades of errors limit predictability
- Cloud-resolving simulations are most skillful

Supporting Information:
- Readme
- Figures S1–S4

Correspondence to:
L. R. Leung,
ruby.leung@pnnl.gov

Citation:
Taraphdar, S., P. Mukhopadhyay, L. R. Leung, F. Zhang, S. Abhilash, and B. N. Goswami (2014), The role of moist processes in the intrinsic predictability of Indian Ocean cyclones, *J. Geophys. Res. Atmos.*, *119*, 8032–8048, doi:10.1002/2013JD021265.

Received 27 NOV 2013
Accepted 7 JUN 2014
Accepted article online 11 JUN 2014
Published online 12 JUL 2014

The role of moist processes in the intrinsic predictability of Indian Ocean cyclones

S. Taraphdar[1], P. Mukhopadhyay[2], L. Ruby Leung[1], Fuqing Zhang[3], S. Abhilash[2], and B. N. Goswami[2]

[1]Pacific Northwest National Laboratory, Richland, Washington, USA, [2]Indian Institute of Tropical Meteorology, Pune, India, [3]Department of Meteorology, Pennsylvania State University, University Park, Pennsylvania, USA

Abstract The role of moist processes in short-range forecasts of Indian Ocean tropical cyclones (TCs) track and intensity and upscale error cascade from cloud-scale processes affecting the intrinsic predictability of TCs was investigated using the Weather Research and Forecasting model with parameterized and explicitly resolved convection. Comparing the results from simulations of four Indian Ocean TCs at 10 km resolution with parameterized convection and convection-permitting simulations at 1.1 km resolution, both reproduced the observed TC tracks and intensities significantly better than simulations at 30 km resolution with parameterized convection. "Identical twin" experiments were performed by introducing random perturbations to the simulations for each TC. Results show that moist convection plays a major role in intrinsic error growth that ultimately limits the intrinsic predictability of TCs, consistent with past studies of extratropical cyclones. More specifically, model intrinsic errors start to build up from the regions of convection and ultimately affect the larger scales. It is also found that the error at small scale grows faster compared to the larger scales. The gradual increase in error energy in the large scale is a manifestation of upscale cascade of error energy from convective to large scale. Rapid upscale error growth from convective scales limits the intrinsic predictability of the TCs up to 66 h. The intrinsic predictability limit estimated by the 10 km resolution runs is comparable to that estimated by the convection-permitting simulations, suggesting some usefulness of high-resolution (~10 km) models with parameterized convection for TC forecasting and predictability study.

1. Introduction

Although midlatitude weather systems are relatively well forecasted by numerical weather prediction models, forecasting tropical weather systems remains challenging. Tropical cyclones (TC) are major components of tropical weather systems that are also the costliest and deadliest natural hazards in the tropics [*Pielke et al.*, 2008]. Over the past few decades, significant progress has been made in forecasting TC tracks but there is virtually little improvement made in intensity forecasts [*Houze et al.*, 2007]. Therefore, model skill in predicting TC formation and rapid intensification and decay is still very limited [*Elsberry et al.*, 2007]. A better understanding of error growth in TC forecasts can potentially lead to improved methods and modeling for TC forecast [*Van Sang et al.*, 2008].

One reason why predicting TC intensity is difficult is because it is largely determined by far less predictable internal dynamics that is modulated by the large-scale environment [*Holland*, 1997; *Emanuel*, 1999]. The upscale growth of moist convection in the form of vertical hot towers or convection-induced vorticity anomalies may play a major role in the internal dynamics [*Hendricks et al.*, 2004; *Krishnamurti et al.*, 2005; *Fang and Zhang*, 2010, 2011]. Furthermore, heating released from tropical clouds and their large-scale organization by the Madden-Julian Oscillation [*Madden and Julian*, 1971, 1994; *Zhang*, 2005] or monsoon intraseasonal oscillations [*Goswami et al.*, 2003] is one of the main driving forces for tropical weather such as lows, depressions, and TCs [*Rosenthal*, 1978; *Wu and Wang*, 2001; *Wang*, 2009]. Hence, the fidelity of models in simulating tropical cloud clusters and their variability is crucial in the prediction of TCs at all time scales. Current climate models have serious problems in simulating tropical clouds and their variability [*Lin et al.*, 2006, 2008] because of uncertainties in parameterizations of convection. It appears that global cloud-resolving models may be necessary to simulate tropical cloud clusters and their large-scale organization. Success of the Nonhydrostatic ICosahedral Atmospheric Model in simulating some of the tropical cloud features realistically [*Miura et al.*, 2007; *Oouchi et al.*, 2009; *Sato et al.*, 2009; *Liu et al.*, 2009] seems to support such a conjecture. As clouds predominantly govern the large-scale tropical heating distribution, very high-resolution models (even cloud-resolving) may be required for climate simulation and prediction [*Shukla et al.*, 2009].

However, even using cloud-scale models for prediction poses a number of challenges. As individual clouds develop as a result of convective instability, which has a much faster growth rate compared to the growth rate of weather disturbances, upscale cascade of errors in the cloud scale can, in principle, ultimately limit the predictability at mesoscales and beyond [*Zhang et al.*, 2002, 2006; *Zhu and Thorpe*, 2006; *Walser and Schär*, 2004; *Hohenegger et al.*, 2006; *Bei and Zhang*, 2007; *Mapes et al.*, 2008]. Moreover, the predictability for phenomena at storm scale or cloud scale is not only controlled by the underlying dynamical and physical processes of the background flow but also by the representations of these processes in the forecast model [*Fuhrer and Schär*, 2005; *Martin and Xue*, 2006; *Farby*, 2006]. The intrinsic predictability (i.e., the extent to which prediction is possible even with a "perfect" model and error-free observations) of warm-season weather that produced flooding events in southern Texas and along the Mei-Yu front in China has been studied by *Zhang et al.* [2006] and *Bei and Zhang* [2007], respectively. They found that small-scale error growth is strongly nonlinear and upscales rapidly due to moist processes. Similarly, moist convection may also limit the skills of hurricane intensity prediction, as shown by *Sippel and Zhang* [2008, 2010] and *Zhang and Sippel* [2009].

Both model resolution and representation of moist processes have been longstanding issues in mesoscale predictability. Consistent with the study of *Zhang et al.* [2002, 2003] for winter snowstorm, *Clark et al.* [2010] found a larger error growth for spring time weather in higher-resolution convection-permitting model (4 km) compared to model with parameterized convection (20 km) for an ensemble of simulations with perturbed lateral and boundary conditions. More recently, *Wang et al.* [2012] examined how the complexity of microphysical schemes influences predictability of warm-season convection over central United States using a model with cloud-permitting resolution. They found that the simplest and the most complex schemes shared similar error growth rate of initial perturbations, suggesting that error growth is intrinsic to the nonlinearity in the moist dynamics. On the other hand, a recent study of *Mukhopadhyay et al.* [2011] demonstrated that models at 10 km grid spacing with parameterized convection could simulate TCs over the Indian region more realistically than using cloud-permitting resolution of 3.3 km grid spacing. Hence, it remains unclear how models with parameterized convection behave in terms of model intrinsic error growth characteristic compared to convection-permitting simulations. As global cloud-resolving models require enormous computational resources, it is important to establish whether such models may advance the skill of tropical weather forecasts or their skills may be limited by the upscale contribution of errors from the smallest scales.

This study investigates the model intrinsic error growth characteristics for TCs over Indian Ocean using a regional model with a sufficiently large spatial domain through a suite of "identical twin" perturbations experiments similar to approaches reported by earlier studies [*Islam et al.*, 1993; *Hohenegger and Schar*, 2007; *Zhang et al.*, 2007; *Taraphdar et al.*, 2010]. Our goals are to understand the mechanism behind the error cascades of Indian Ocean TC within the different scales and to examine possible differences in estimating the inherent intrinsic error growth from mesoscale simulations that rely on convective parameterizations versus convection-permitting simulations. The latter has important implications to numerical design for TC analysis, prediction, and predictability. We selected four cases of TCs over the Bay of Bengal (BOB) that were associated with vigorous convective activities and strong convective feedback. The experimental design is described in section 2. Results are discussed in section 3, and findings are summarized in section 4.

2. Experimental Settings

2.1. Model Configurations

The nonhydrostatic compressible WRF-ARW (Advanced Weather Research and Forecasting) model version 3.4 is used with 35 vertical terrain following levels with the model top at 10 hPa. The model configuration consists of a large single domain at 10 km and 30 km horizontal resolution, respectively, that covers 2°S to 36°N and 62°E to 109.5°E. In addition, simulations have also been performed with a nested configuration using the large 10 km resolution domain as the outer domain, but includes a smaller domain at 3.3 km grid spacing extending from 7°N to 28.5°N and 77.5°E to 101°E, and an innermost domain at 1.1 km grid spacing covering 9°N to 26.5°N and 80°E to 98°E (Figure 1a), with the three domains all two-way nested to telescopically zoom into 1.1 km resolution for simulating the TCs.

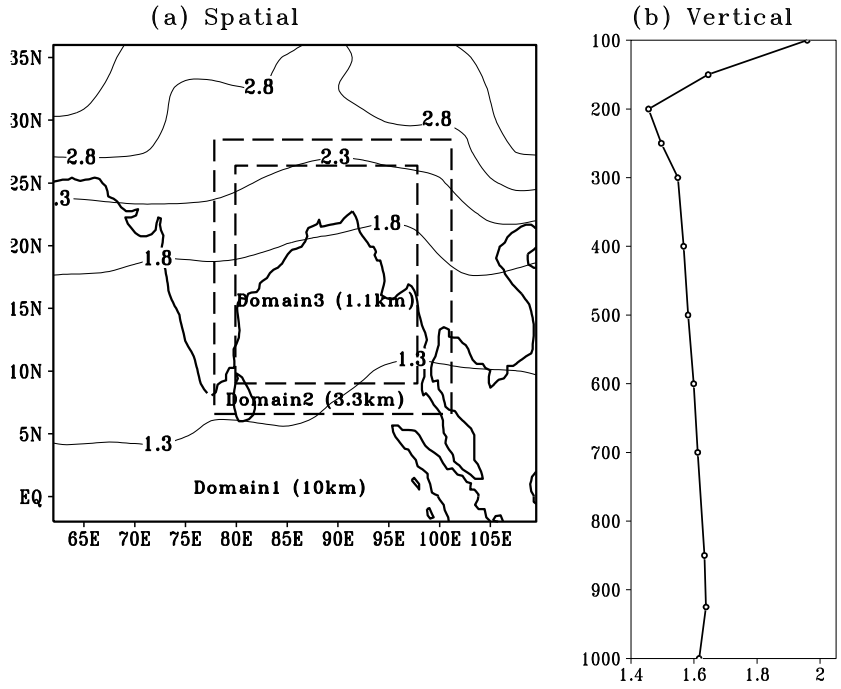

Figure 1. The WRF 500 × 400 mother domain at 10 km resolution and the two-way triple nested fine domain (716 × 783; Domain 2) at 3.3 km resolution and the innermost domain (1800 × 1750) at 1.1 km resolution. Simulations have also been performed using a single 10 km resolution domain (500 × 400) and a single 30 km resolution domain (167 × 133) covering the same area as Domain 1. (a) The standard deviation of premonsoon and postmonsoon (April, May, October, and November) temperature climatology vertically averaged between 1000 and 100 hPa. (b) The vertical distribution of the average temperature over the dashed inner box.

For the large domain at 10 km and 30 km resolution, cumulus convection is parameterized using the Kain-Fritsch (KF) scheme [*Kain and Fritsch*, 1990, 1993] while the WRF Single Moment 6-Class Microphysics (WSM6) [*Dudhia et al.*, 2008] scheme is chosen for the cloud microphysical processes. Although the choice of cumulus or cloud microphysics schemes is not critical in identical twin experiments, our earlier study [*Mukhopadhyay et al.*, 2011] indicates that the KF scheme produces a better simulation of TC track and intensity over the BOB. In the nested configuration, KF is used in the outer domain at 10 km resolution, but no cumulus parameterization is used in the 3.3 km and 1.1 km resolution domains since convection is explicitly resolved at the high resolution. The Rapid Radiative Transfer Model scheme based on *Mlawer et al.* [1997] is used for longwave radiation, and the *Dudhia* [1989] scheme is used to parameterize shortwave radiation. The surface layer parameterization [*Janjic,* 2002] is based on the similarity theory [*Monin and Obukhov*, 1954]. The viscous sublayer is parameterized following *Janjic* [1994] over water and land. The MM5 5-layer soil temperature thermal diffusion model is used to represent land surface effects. For the planetary boundary layer, the Yonsei University scheme is used with the counter gradient terms to represent turbulence fluxes due to nonlocal gradient. The various model configurations summarized in Table 1 allow comparisons of intrinsic error growth in simulations with parameterized convection and in convection-permitting simulations in which no cumulus parameterization is used.

2.2. Data and Methodology

The National Center for Environmental Prediction-Global Forecasting System analyses and forecasts available at 6-hourly intervals are used to provide initial and boundary conditions for the simulations. Each case of TCs includes two types of simulation—control and perturbation experiments. In the control run, the model is initialized about 3 days before the TCs reach their maximum intensity and integrated for 96 h to cover the total life cycle of TC. Eight "perturbed" integrations are carried out for each "control" run by introducing small random perturbations in the temperature field of the initial conditions for each experiment. To

Table 1. Details of the Numerical Experiments and Their Control Counterpart (Mentioned Within the Bracket) for All Tropical Cyclone Cases

Experiment Name	Domains and Resolution	Cumulus Scheme	Cloud Microphysics Scheme	Perturbations	Comments
Fake dry	10 km Single Domain	None	WSM6, but no feedback to circulation	Whole domain	Fake Dry Experiment
Exp-10 km (ctl-10 km)	10 km Single Domain	KF	WSM6	Whole domain	Parameterized convection and cloud microphysics, Perturbations applied to the whole domain
Exp-30 km (ctl-30 km)	30 km Single domain	KF	WSM6	Whole domain	Same as the 10 km experiment but at 30 km resolution
Exp-1.1 km (ctl-1.1 km)	Two-way triple nested with three domains at 10 km, 3.3 km, and 1.1 km resolution	KF (d1) None (d2) None (d3)	WSM6 (d1) WSM6 (d2) WSM6 (d3)	All domains	Here d1, d2, and d3 stand for domains at 10 km, 3.3 km, and 1.1 km resolution, respectively, with d1 covering the same region as the 10 km single domain
Exp-1.1 km PertD3	Same as exp-1.1 km	KF (d1) None (d2) None (d3)	WSM6 (d1) WSM6 (d2) WSM6 (d3)	Only in the inner most domain	Same as exp-1.1 km but perturbations are applied only in the inner most domain

determine the amplitude of the perturbations, the spatial and vertical distributions of the standard deviation of temperature for the premonsoon and postmonsoon months (April, May, October, and November) are shown in Figures 1a and 1b. Perturbations are computed using a random number generator with zero mean and unit standard deviation and multiplied by amplitude values of ±0.01 K, ±0.02 K, ±0.025 K, ±0.04 K, ±0.05 K, ±0.06 K, ±0.075 K, and ±0.1 K, respectively. Note that the random perturbations have amplitudes far smaller than typical observation or analysis errors. The perturbations are then added to the three dimensional temperature before the initialization procedure. So for each control simulation there are eight perturbed simulations with equal weighting given to each perturbed member to construct the ensemble. Since the mean of the perturbations is zero, no systematic biases are introduced in the initial time of the simulations. In order to identify the source of error growth, we have analyzed the composited 32 "perturbation" experiments (eight perturbations applied to each of the four TCs) for all the results reported below.

Before doing the perturbation experiments, control experiments are first performed for four TC cases with three different configurations including ctl-30 km and ctl-10 km that use the large single domain with parameterized convection, and ctl-1.1 km that used a nested configuration to explicitly resolve convection. The control integrations are compared with observations including minimum sea level pressure (SLP), maximum wind speed, and track data from the India Meteorological Department report and precipitation data from TRMM3B42 [*Huffman et al.*, 2007]. The simulations show realistic features comparable to the observations and provide confidence for the perturbation experiments. For each control experiment, eight perturbation experiments with different amplitudes of random perturbations are performed for each TC using the same model configuration of the control experiments (i.e., 30 km, 10 km, and 1.1 km, respectively). The simulations with random perturbations are called exp-30 km, exp-10 km, and exp-1.1 km, respectively. In addition, one more set of experiment called "Fake Dry experiment" is performed using the 10 km resolution single large domain in which the latent heating source is removed in both the control and perturbation experiments. Details of the fake dry experiments are given in section 3.2. The composited analyses are presented in the following sections. When different experiments at different model resolutions are compared, the variables are interpolated to a common grid at 10 km resolution.

For diagnosing error growth between the control and perturbed simulations, we define the difference total energy (DTE) and difference kinetic energy (DKE) as follows:

$$\mathrm{DTE} = \frac{1}{2}\sum_{ijk}\left(U'^{2}_{ijk} + V'^{2}_{ijk} + \kappa T'^{2}_{ijk}\right). \quad (1)$$

$$\mathrm{DKE} = \frac{1}{2}\sum_{ijk}\left(U'^{2}_{ijk} + V'^{2}_{ijk} + W'^{2}_{ijk}\right). \quad (2)$$

where U', V', W' and T' are the differences of wind components and temperature between the control and perturbed runs, with i, j, and k sum over the grid points in the x, y, and z directions and $\kappa = \mathrm{Cp/Tr}$, where Tr is the reference temperature of 270 K. Power spectra of the DTE at different times are also calculated to examine the upscale cascade of error energy from smaller to larger scales. The 2-D spectral decomposition using the fast Fourier transform (FFT) algorithm is first performed for U', V' and T' at each vertical level, and then the spectrum power density is calculated for each wave number and integrated vertically following *Zhang et al.* [2002, 2003, 2007].

To estimate the intrinsic predictive time scale of the model within the TC environment, the error doubling time is computed as follows (similar to *Islam et al.* [1993]). First, the loss of information in the forecast is quantified as a function of time elapsed since the perturbation. This essentially is used as a measure of intrinsic predictability in time. The spatially averaged prediction error E_{ij} (t) is defined as follows

$$E_{ij}(t) = \left\{ \frac{1}{N_x N_y} \sum_{i=1}^{N_x} \sum_{j=1}^{N_y} \left[C_{i,j}(t) - P_{i,j}(t) \right]^2 \right\}^{1/2} \tag{3}$$

where $C_{i,j}(t)$ and $P_{i,j}(t)$ are, respectively, the variables (e.g., rainfall, DTE) for the control and perturbed experiments at a spatial location (i, j). N_x and N_y are the number of grid points along the x and y directions. As an estimate of the natural variability of the processes, the standard deviation of the control parameters (e.g., rainfall) σ_c as a function averaged over space and time is used,

$$\sigma_c = \left[\frac{1}{N_x N_y N_t} \sum_{k=1}^{N_t} \sum_{i=1}^{N_x} \sum_{j=1}^{N_y} \left(C_{i,j,k} - \overline{C} \right)^2 \right]^{1/2} \tag{4}$$

where the subscript k denotes time and N_t is the total number of time steps. $\overline{C}$ denotes the mean of the parameters in the control experiment.

The time it takes for the ratio of $\frac{E^2}{\sigma_c^2}$ to reach the magnitude of 2 ("error doubling time") is used as a measure of the intrinsic predictive time scale for the model.

2.3. Brief Overview of Synoptic Scale Conditions During the Tropical Cyclone Cases

We selected four TC cases over the BOB representing different intensities—the very severe cyclone "SIDR" (2007), the severe cyclone "AILA" (2009), the cyclone "BIJLI" (2009), and the cyclonic storm "RASHMI" (2008). SIDR formed over southeast BOB and its neighborhood on 11 November 2007 and intensified into cyclone by the next day. SIDR was a category 5 TC in the Saffir-Simpson scale that resulted in one of the worst natural disasters in Bangladesh. AILA initially formed as a depression over southeast BOB at 06 UTC of 23 May 2009 and under very favorable conditions rapidly intensified into cyclone on 24 May. A special feature of this cyclone is that it crossed the coast as a severe tropical cyclone and maintained its intensity even after landfall. BIJLI formed over the southeast and east-central BOB on 14 April 2009, which is climatologically rare over BOB, moved north-northeast and intensified into cyclone. This cyclone gradually weakened prior to landfall and caused moderate damages over Bangladesh. Under the influence of favorable large-scale conditions, RASHMI developed on 25 October 2008 near 16.5°N and 86.5°E. RASHMI was a fairly weak TC, it still caused some notable damage in Bangladesh and India. The selected TC cases represent a wide variety of strength from very severe cyclones to very weak tropical storms, and they developed under different large-scale conditions. This allows us to study model error growth representative of TCs in the Indian Ocean more generally. More details of each cyclone and its environmental conditions (Figures S1 and S2 in the supporting information) are given in the supporting information.

3. Results

3.1. Track and Intensity Forecast of TCs in Control Experiments

The single large domain control experiments are conducted at 10 km (ctl-10 km) and 30 km (ctl-30 km) horizontal resolutions with both convective parameterizations and cloud microphysics for the simulations of

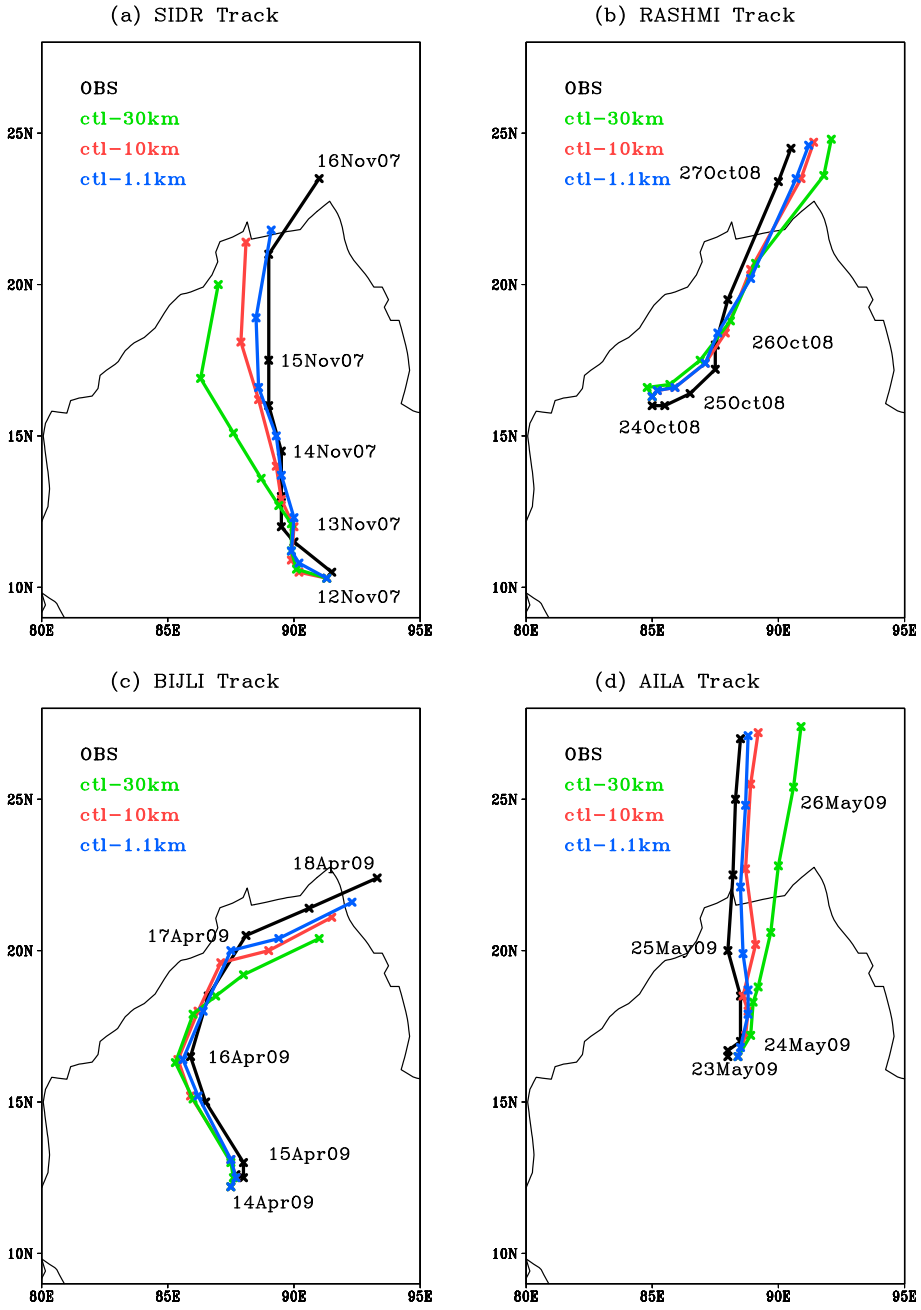

Figure 2. The 96 h forecasted tropical cyclone track from (a) SIDR, (b) RASHMI, (c) BIJLI, and (d) AILA for Observation (black), ctl-10 km (red), ctl-30 km (green), and ctl-1.1 km (blue).

four TCs over BOB. Similar cases are also run with the convection-permitting simulations at 1.1 km (ctl 1.1 km) resolution that used only cloud microphysics representation but not cumulus parameterization. The simulated tracks of the four TCs in all the control experiments (ctl-30 km, ctl-10 km, and ctl-1.1 km) are compared against observations in Figures 2a–2d. The simulated tracks are very realistic for all the TC cases except for SIDR in the ctl-30 km experiment in which the tracks are very close to observation for the first 2 days but deviate thereafter. Comparing the various simulations, it is clear that the tracks are closer to observations in ctl-10 km and ctl-1.1 km than ctl-30 km, with ctl-1.1 km reproducing the observed tracks the best.

The time evolutions of minimum sea level pressure and maximum sustained 10 m winds are shown in Figure 3. The ctl-10 km and ctl-1.1 km simulations clearly outperform the ctl-30 km simulations in cyclone

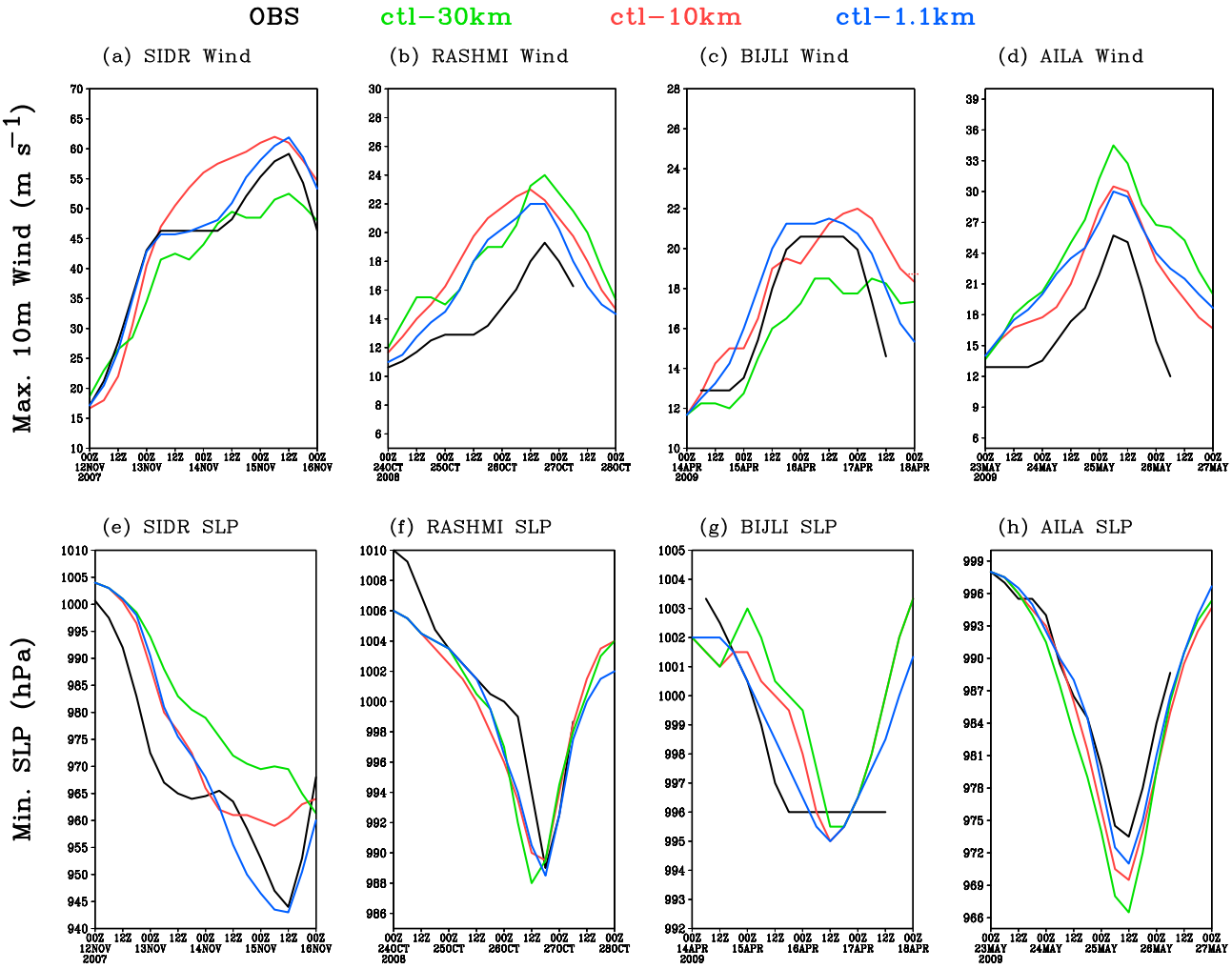

Figure 3. The time evolution of (a–d) maximum sustainable 10 m wind and (e–f) minimum SLP for SIDR, RASHMI, BIJLI, and AILA, respectively, from Observation (black), ctl-30 km (green), ctl-10 km (red), and ctl-1.1 km (blue).

intensity, which is too low for the strong case (SIDR). The high-resolution ctl-1.1 km simulation again outperforms other simulations in intensity. The daily evolutions of spatial distribution of reflectivity (proxy for clouds) for all four TC cases in ctl-1.1 km and ctl-10 km are shown in Figures S3 and S4, respectively. They clearly show that among the four cases, SIDR and AILA both reached the very severe (64–119 kt) to severe (48–63 kt) cyclone stage while the other two cases remain in the cyclonic storm stage (34–47 kt). The simulations at both resolutions capture the TC features, but more detailed structures can be seen in ctl-1.1 km (Figure S3).

To quantitatively compare the performance of different resolutions, we computed the normalized pattern statistics for the minimum sea level pressure and maximum 10 m wind (Figure 4a). The results are presented in the Taylor diagram [*Taylor*, 2001] in which the distance from the origin indicates the normalized standard deviation, and the cosine of the angle of the position vector indicates the pattern correlation between the observed and simulated variable. The distance from the reference point (marked as "REF") to the plotted points denotes the root-mean-square error (RMSE). The results clearly show that the ctl-1.1 km simulations have the minimum RMSE and maximum correlation, and the variability is also very similar to observation. The 30 km simulations are the least skillful among the three experiments with different resolutions. The composited daily track errors (Figure 4b) also support the better performance of ctl-1.1 km resolution as seen by the smaller track errors than the other two lower resolution runs. All the above analyses

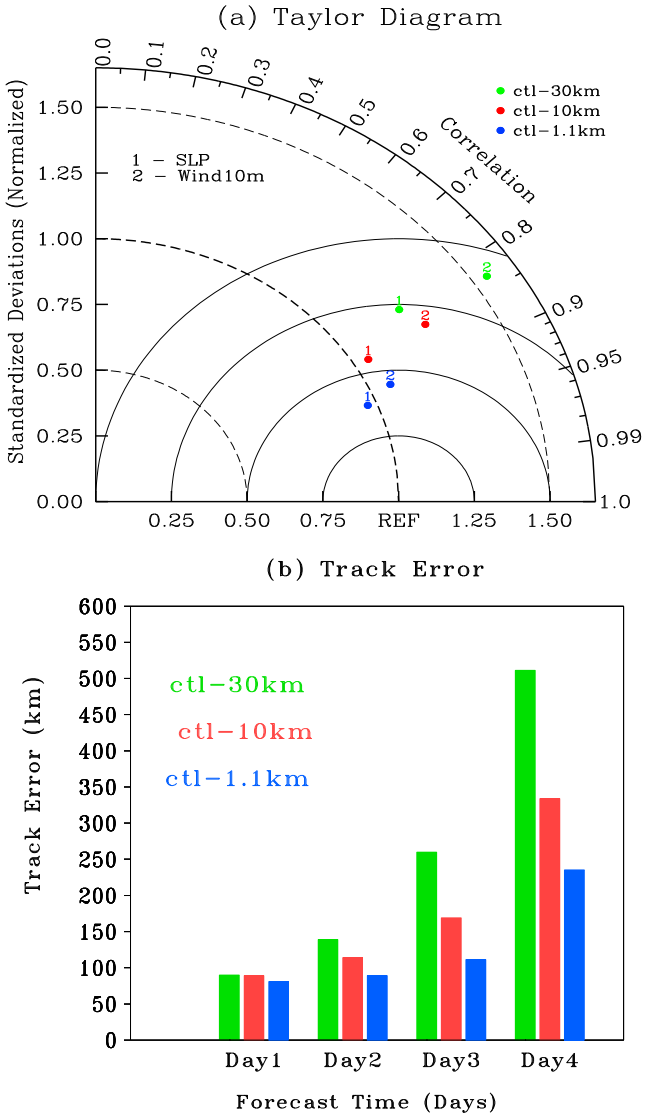

Figure 4. (a) The composited (four TC cases) normalized pattern statistics difference (Taylor diagram) comparing simulations at three different resolutions (30 km, green; 10 km, red; and 1.1 km, blue) with observations for the sea level pressure (SLP) and 10 m wind. REF indicates as a reference point. The numbers "1" and "2" refer to SLP and 10 m wind, respectively. (b) The composited daily track error for simulations at the above three different resolutions.

quantitatively suggest that the ctl-1.1 km simulations outperform the other two (10 km and 30 km) simulations with respect to storm track and intensity (Figures 2–4). These results suggest that adequate resolution is necessary to realistically resolve the processes such as eyewall dynamics and spiral rain bands that control the TC intensity.

Despite being inferior to ctl-1.1 km, the 10 km simulations still realistically capture the observed TC tracks and intensities for the four TC cases through the use of a convective parameterization. However, as the resolution is further degraded, ctl-30 km is noticeably less skillful than ctl-10 km even with the cumulus parameterization. Given the inherent uncertainties in the representation of moist processes in the forecast model, the divergence among the different control simulations shows the limit of practical predictability for deterministic prediction of Indian Ocean TCs. In the following sections we use DTE and precipitation (both as a proxy of intensity) to quantify the error growth and focus on estimating the intrinsic predictive time scale of a low- and high-resolution convection-permitting model within the TC environments under different model configurations.

3.2. Role of Diabatic Heating in Error Growth in Short-Range Forecasts

Before investigating in more detail the role of moist convection in the short-range model forecast of TC, the importance of diabatic heating in error growth should be established. A "fake dry" experiment is carried out with 10 km grid spacing in which all the sources of diabatic heating associated with moisture are absent compared to the standard experiment (exp-10 km) at the same resolution. So in the fake dry experiment, convective parameterization is turned off and the latent heating associated with microphysical processes is not added to the prognostic equations so the large-scale wind, moisture, or temperature fields are not influenced by latent heating. The composite normalized DTE averaged over 85°–95°E and 12°–24°N for exp-10 km and fake dry is shown in Figure 5a. Since the variability of the full-moist experiments is much larger than that of the fake dry experiments, the DTE of each experiment is normalized by its own natural variability for a more meaningful comparison. As an estimate of the natural variability of the DTE, the standard deviation of the DTE as a function averaged over space and time is used. It is interesting to note that the normalized DTE grows significantly faster and the normalized errors are also much higher in exp-10 km than fake dry.

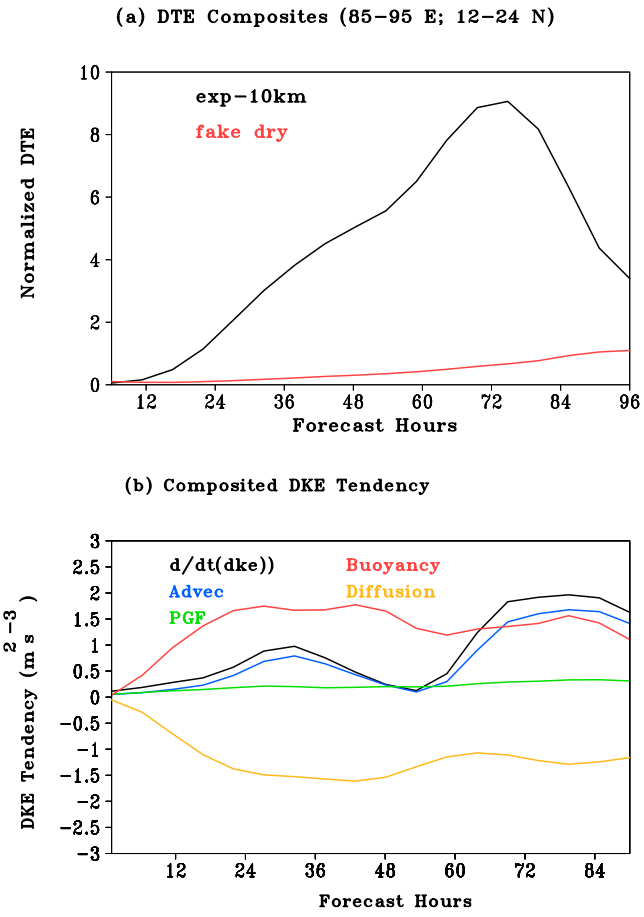

Figure 5. Time evolution of normalized Difference of Total Energy (DTE) in exp-10 km (black line) and fake dry (red line) at 10 km resolution averaged over 85°–95°E and 12°–24°N. Normalization is performed with respect to the natural variability. (b) The time evolution of DKE tendency ($m^2 s^{-3}$) and each of the source/sink term estimated from the 10 km grids in exp-10 km. Vertical integration is done between 950 and 150 hPa in both panels.

Furthermore, the error in the moist experiment (exp-10 km) follows closely the life cycle of the TCs (from initial growth to reach peak intensity and eventual decay), but the error in the fake dry experiment slowly increases most likely due to (dry) hydrodynamic instabilities of the background flow. Consistent with past studies on the error growth of midlatitude extratropical cyclones [*Zhang et al.*, 2003, 2007], it is clear that error growth comes predominantly from the moist convective processes rather than from dry hydrodynamic instabilities of the background flow. This motivates further experiments to study the role of moist processes on the error growth in short-range forecasts.

3.3. Budget Analyses of Difference Kinetic Energy

To further quantify the influence of moist convection and other inherent physical processes on the error growth from convective to synoptic scales, a budget analysis of the difference kinetic energy (DKE) between exp-10 km and its control experiment is performed. The budget tendency equation is written in terms of different source and sink terms following *Zhang et al.* [2007].

$$\frac{\partial}{\partial t}(\mathrm{DKE}) = -\rho_0\left[U'\delta(V\cdot\nabla u) + V'\delta(V\cdot\nabla v) + W'\delta(V\cdot\nabla w)\right] - \rho_0\left[U'\delta\left(\frac{1}{\rho}\frac{\partial p}{\partial x}\right) + V'\delta\left(\frac{1}{\rho}\frac{\partial p}{\partial y}\right) + W'\delta\left(\frac{1}{\rho}\frac{\partial p}{\partial z}\right)\right]$$
$$-\rho_0\left[\frac{g}{\theta_0}W'\theta' - g(\delta q_c + \delta q_r)w\right] + \rho_0\left[U'\delta D_u + V'\delta D_v\right] + \rho_0\left[W'\delta D_\omega\right] \quad (5)$$

where DKE is defined in equation (2) and U', V', W' and θ' are the differences of wind components and potential temperature between the control and perturbed runs, and $\delta(.)$ represents the difference between the two sets of simulations.

The source and sink terms include nonlinear velocity advection (first bracket in the right-hand side of equation (5)), net contribution by pressure gradient force (second bracket), buoyancy generation and dissipation (third bracket), and dissipation due to horizontal and vertical diffusion (fourth and fifth brackets). The domain averaged time evolution of the DKE tendency along with each source/sink term is computed from exp-10 km and shown in Figure 5b. The source term that dominates the tendency is found to be the buoyancy (red; Figure 5b) and nonlinear velocity advection (blue). The dominant sink term is the total diffusion (vertical and horizontal; yellow). Figure 5b clearly shows that buoyancy dominates the DKE tendency until 60–66 h of forecast when the TC forms and reaches its maximum strength. After 72 h of forecast, advection and buoyancy are similar in magnitude when the TC is at the dissipation phase and

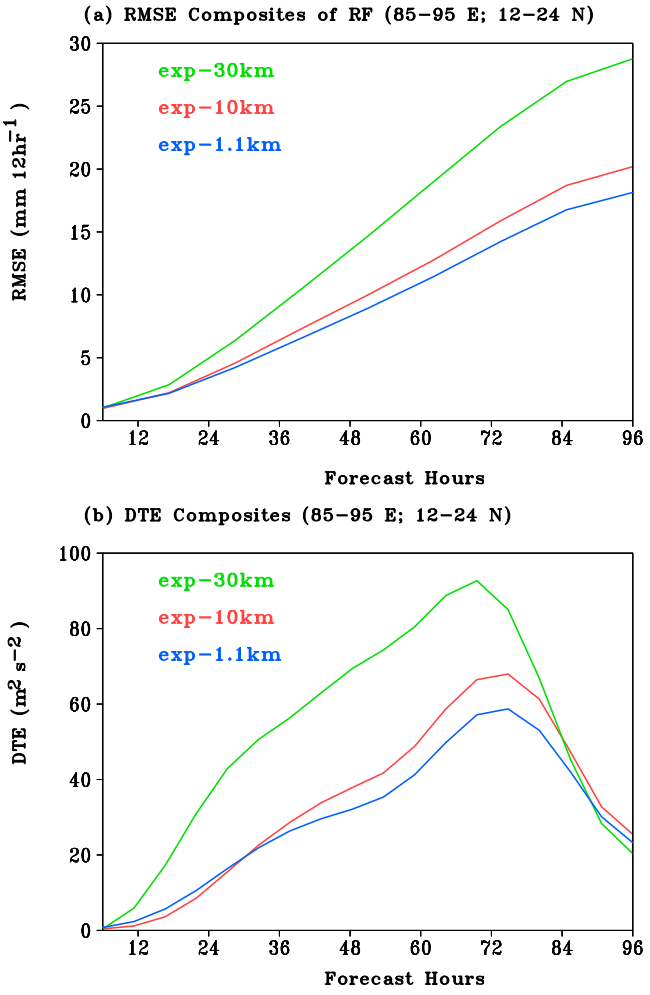

Figure 6. Time evolution of the (a) root-mean-square error for rainfall (mm 12 h^{-1}) and (b) DTE (m^2 s^{-2}) in exp-10 km (red line), exp-30 km (green line), and exp-1.1 km (blue line) averaged over 85°–95°E and 12°–24°N.

convection slowly dissolves. It is well established that buoyancy is related to diabatic heating of the model; and therefore, it is associated with moist convection [*Zhang et al.*, 2007]. The DKE budget analysis confirms that buoyancy associated with moist convection dominantly controls the error growth in these TC events over the Indian region.

3.4. Impact of Model Resolution in the Error Growth of Short-Range Forecasts

To understand the impact of model horizontal resolution and representation of moist processes on the model-estimated intrinsic error growth, three sets of experiments are analyzed including simulations conducted using the single large domain at 30 km and 10 km grid spacing with parameterized convection (i.e., exp-30 km and exp-10 km) and the convection-permitting simulations performed at 1.1 km grid spacing (exp-1.1 km) without any cumulus convection parameterization. All the experiments include their own control simulation and the "perturbations" counterparts for all four TC cases. The composited (8 perturbations × 4 cases = 32 samples) analyses are presented in the sections that follow.

To quantify the impact of model resolution and representation of moist processes on the estimation of the error growth, the time evolution of RMSE of precipitation (mm 12 h $^{-1}$) and DTE (m^2 s^{-2}) for exp-10 km (red line), exp-30 km (green line), and exp-1.1 km (blue) is shown in Figures 6a and 6b, respectively. The RMSE of precipitation (Figure 6a) in exp-10 km (red) and exp-1.1 km (blue) is much lower than exp-30 km (green) throughout the forecast period except in the initial 12–18 h when all simulations are influenced by similar initial conditions. The DTE (Figure 6b) also increases for all experiments until 72 h of forecasts. These results suggest that increased horizontal resolution in simulations with parameterized convection or explicitly resolving convection can limit the error buildup in the model. Having established the importance of higher resolution in mesoscale simulations with parameterized convection, we focus our analyses on only exp-10 km and exp-1.1 km to further elucidate error growth and predictability of TCs and compare simulations with parameterized versus explicitly resolved convection.

3.5. Impact of Moist Convection Parameterizations in the Error Growth of Short-Range Forecasts

Next we compare the impact of moist physics on intrinsic error growth of TCs in simulations with parameterized (exp-10 km) and explicitly resolved (exp-1.1 km) convection. This has important implications to the design of numerical forecasting of TCs. We start our measures of intrinsic error growth in terms of the intrinsic predictive time scale. Computations of the intrinsic predictive time scales are given in the data and methodology section 2.2. It is found in Figure 7 that the intrinsic predictive time scales for the

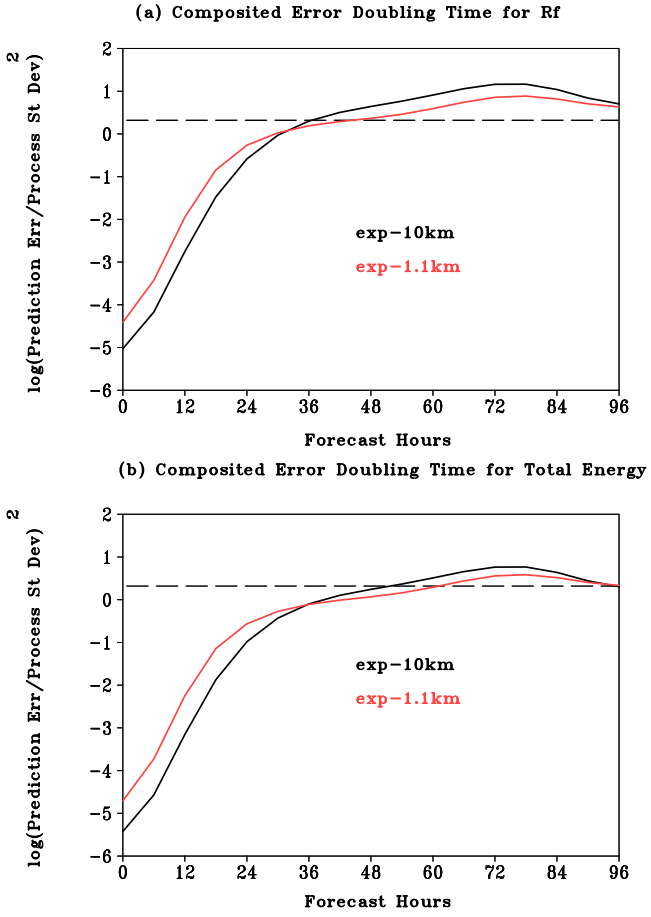

Figure 7. Time evolution of predictive time scale (*y* axis in log scale) for exp-10 km (black line) and exp-1.1 km (red line) for (a) precipitation and (b) Total Energy averaged over 85°–95°E and 12°–24°N.

experiments (i.e., exp-10 km (black line) and exp-1.1 km (red line)) are surprisingly very close to each other except for a slightly longer predictive time scale for exp-1.1 km. The exp-1.1 km has an intrinsic predictive time scale of around 42 h for precipitation (Figure 7a; red line) and 66 h for total energy (Figure 7b; red line) compared to 36 h for precipitation (Figure 7a; black line) and 54 h for total energy (Figure 7b; black line) in exp-10 km. To understand the dependence of the predictable time scale on the respected events, as an example, we computed it for total energy separately for all the cases, e.g., SIDR, BIJLI, AILA, and RASHMI and are found to be 78 h, 72 h, 60 h, and 54 h, respectively, in exp-1.1 km. This suggests that predictable time scale has a considerable variability and strong dependence on the respective events as suggested by *Zhang and Sippel* [2009].

Notably, the above analysis shows that the intrinsic error growth estimated by exp-10 km with parameterized convection is a good representation of the intrinsic error growth estimated by the convection-permitting experiments. This is consistent with Figures 2–4 that show comparable skill in ctl-10 km and ctl-1.1 km in simulating TC tracks and intensities. We note that convective precipitation contributes to 40–50% of the total precipitation in ctl-10 km, so similarity between error growth in ctl-10 km and ctl-1.1 km suggests that the convective parameterization applied at the 10 km resolution reasonably captured the behavior of the convection resolvable with the 1.1 km grid spacing. Daily evolution of the spatial distribution of DTE presented in Figure 8 for exp-10 km and exp-1.1 km clearly shows that the errors in both exp-10 km and exp-1.1 km start to build up mainly in the vicinity of the center of convection (i.e., composite tracks of the TCs) and gradually spread to other areas of the domain, subsequently contaminating the whole domain. The spatial structures of errors from both experiments are similar with slightly higher in amplitude in exp-10 km than exp-1.1 km. Thus, error in the large scales, whether for total energy or precipitation (figure not shown), essentially comes from errors associated with convective processes in both experiments. This suggests the possibility of error energy cascades from smaller to larger scales during the model integration (i.e., from day 1 to day 4) to affect the large-scale predictability. More analyses will be discussed in the following sections to investigate the cascades of errors in the different spatial scales.

3.6. Error Cascades in Different Spatial Scales

To objectively demonstrate error growth at different spatial scales and simultaneously at different lead times, a power spectrum analysis of DTE (Figure 9) is performed for the exp-1.1 km and exp-10 km experiments. Figure 9a shows a sharp increase of DTE until a wavelength of 120–150 km. The DTE has the largest spectral power at around 600 km in wavelength, which is a reflection of the dominant DTE error at the TC

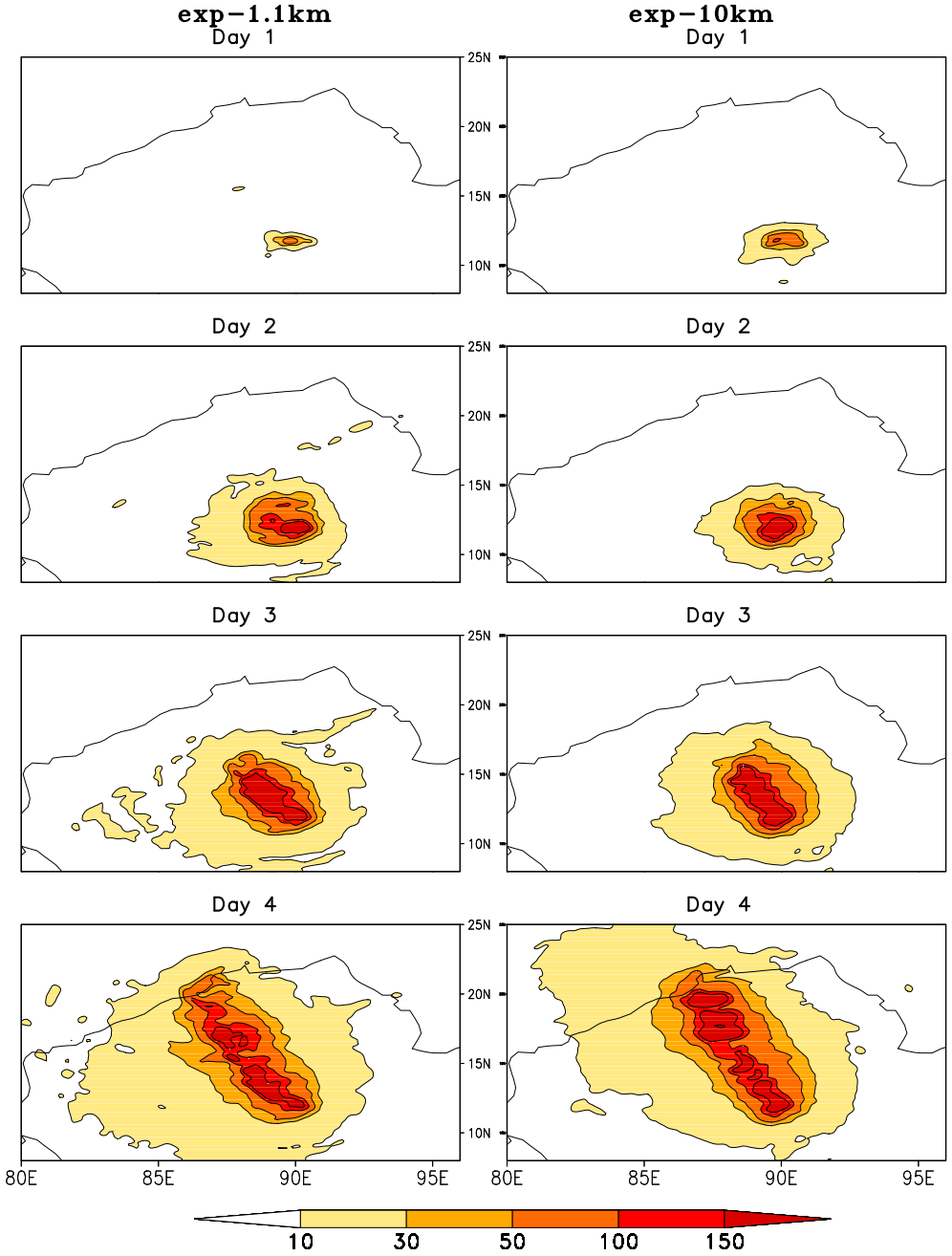

Figure 8. Composites of spatial pattern of Difference of Total Energy (DTE; shaded; $m^2\ s^{-2}$) after the first, second, third, and fourth days of forecast for exp-1.1 km and exp-10 km, respectively. Vertical integration is done between 1000 and 100 hPa.

system scale [e.g., *Fang and Zhang,* 2010, 2011]. Figure 9a also shows that in exp-1.1 km, the error spectra at smaller and intermediate scales (up to 150 km) reach saturation by 12 to 24 h of integration while the error at the TC system scales or larger (>150 km) continues to grow even by Day 4. Figure 9a further shows that the peak of the spectrum gradually shifts from smaller scales to larger scales over time, suggesting cascades of error energy from smaller scales to larger scales as time progresses. Figure 9c plots the time evolution of the DTE peak wavelength, which clearly shifts from smaller to larger wavelength with progression of time, supporting our findings of error energy cascading from smaller scale to larger scale. Experiment exp-10 km (Figure 9b) shows a similar power spectrum of DTE but with higher DTE magnitudes and similar shift from smaller to larger scales as time progresses (Figure 9c) compared to exp-1.1 km.

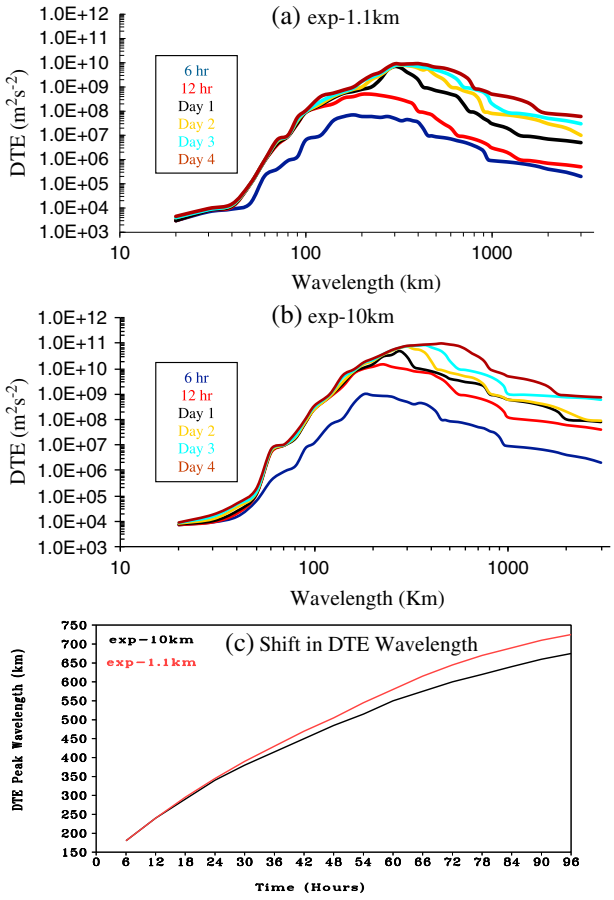

Figure 9. Power spectrum analysis of Difference of Total Energy (DTE; $m^2 s^{-2}$) in (a) exp-1.1 km and (b) exp-10 km after 6 h, 12 h, first, second, third, and fourth day of integration. (c) The time evolution of the DTE peak wavelength (km) for exp-10 km (black line) and exp-1.1 km (red line).

To provide additional insights, one more experiment called exp-1.1 km PertD3 is performed in which perturbations are added only in the convective region (i.e., at smaller scale in domain 3) but not in the larger area outside the convective region in the 3.3 km and 10 km outer domains of the nested configuration. The spatial pattern of the composite DTE (Figure 10a) in exp-1.1 km PertD3 reveals similar buildup of errors found in exp-1.1 km that begin mainly in the vicinity of the center of convection and gradually spread to other areas of the domain by day 2. This suggests that irrespective of the region of perturbation, error always starts to build up from the region of convection and spreads to the larger scales. The cascade of error is further elucidated by analyzing the power spectrum of exp-1.1 km PertD3 (Figure 10b), which is very similar to exp-1.1 km (Figure 9a) and exp-10 km (Figure 9b) in that the error grows from smaller to larger scales indicated by the shift of the peak DTE toward large scales over time. The similarity between the error growth of exp-1.1 km PertD3 and exp-1.1 km is shown more clearly in Figure 10c, except for a smaller DTE magnitude in exp-1.1 km PertD3. This difference in the peak DTE magnitude might be due to sampling error or the randomness of moist convection. Since perturbations are only introduced in the convective region in exp-1.1 km PertD3 but the resulting error energy spectrum is very similar to that of exp-1.1 km, our results further support the error cascades from smaller scale to larger scale that ultimately affect the predictability of the larger scales.

To further illustrate the error growth from smaller to larger scales, Figures 11a–11c shows the time evolution of the map view of the 850 hPa temperature difference (shaded) between two randomly selected ensemble members at different scales for tropical cyclone SIDR. Separations of scales are achieved with a two dimensional spectral decomposition based on FFT [*Lin and Zhang*, 2008; *Fang and Zhang,* 2011]. In the 2-D Fourier decomposition we divided the total wave number into three scale ranges following *Fang and Zhang* [2011] for horizontal scale larger than 150 km (referred as the TC system scale/large scale), between 50 and 150 km (intermediate scale or TC vortex scale), and smaller than 50 km (small scale or the convective scale). At the small scale, large errors are found in areas of moist convection as evident by the spiral structure associated with the cloud bands or eyewall convection (Figure 11a). The error amplitude is apparently approaching the peak at Day 2 (a sign of error saturation) though with some expansion in areal coverage associated with the expansion of the developing TC system.

At the intermediate scale, the temperature structure errors are associated with the inner core vortex in the form of apparent inertial gravity waves and/or mesoscale convective vortices, with some indications of growth in wavelength and intensity from 6 h to Day 4 (Figure 11b). At the system scale, well organized but relatively weak temperature difference (error) distribution can be prominently seen for day 1 onward

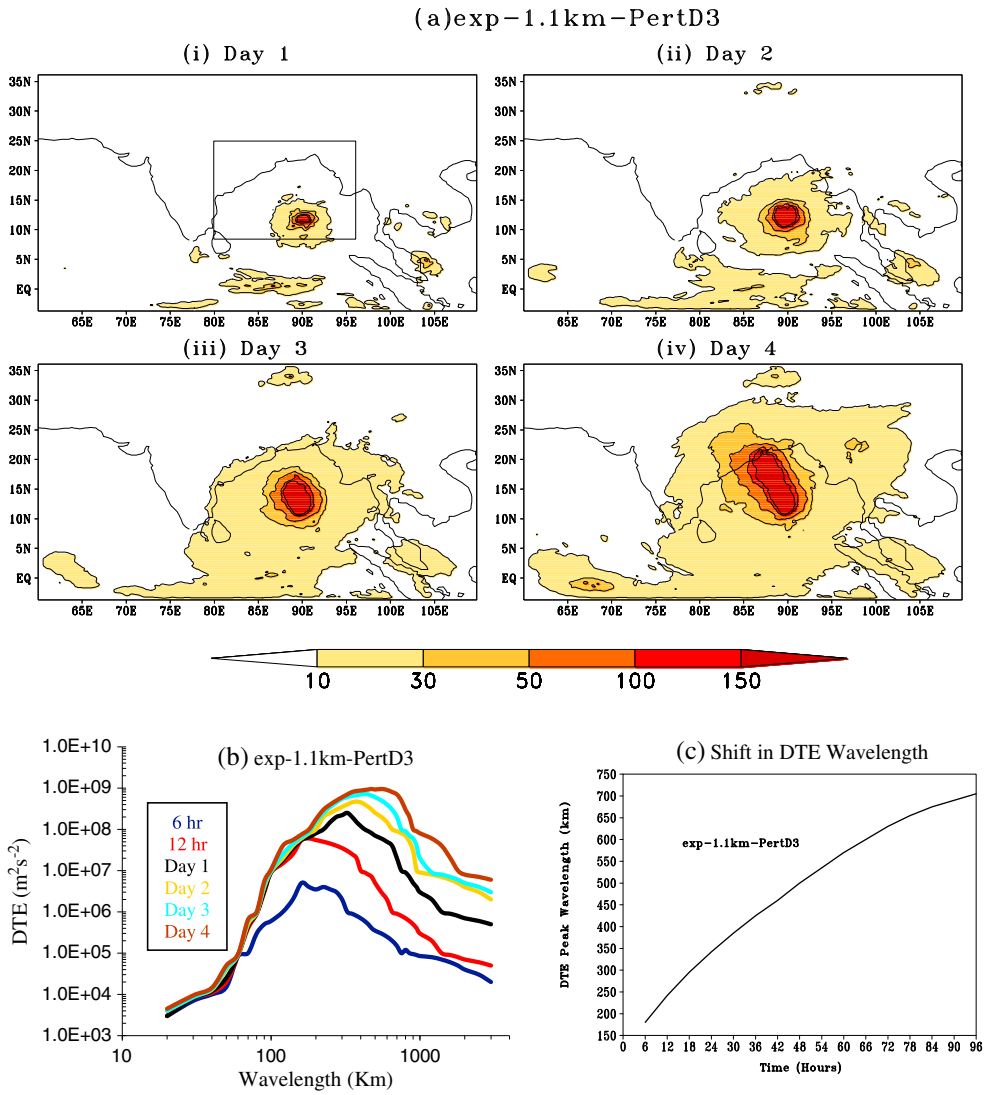

Figure 10. (a) Composite spatial pattern of Difference of Total Energy (DTE; shaded; $m^2 s^{-2}$) after the (i) first, (ii) second, (iii) third, and (iv) fourth days of forecast for exp-1.1 km PertD3. Vertical integration is done between 1000 and 100 hPa levels. The box shown in Figure 10ai indicates the area presented in Figure 8. (b) The power spectrum of DTE at different lead times for the same experiment (exp-1.1 km PertD3) after 6 h, 12 h, first, second, third, and fourth day of integration. (c) The time evolution of the DTE peak wavelength (km) for exp-1.1 km PertD3.

(Figure 11c). This growth and saturation of error from small convective scales to intermediate mesoscale vortex or inertial gravity waves scales and ultimately influence the larger scale (TC system scale) are consistent with the multiscale error growth paradigm developed in *Zhang et al.* [2007] for moist baroclinic waves. The finer scale error growth in the area of moist convection and the intermediate scale error growth in the vortex, followed by errors in the TC system scale are also consistent with the multiscale dynamics of TCs discussed in *Fang and Zhang* [2011]. From the above analyses we can further conclude that the fast nonlinear error growth in the convective region and the cascade of error energy from finer scale to large scale over time are intrinsic in the TCs and limit the ability of models to accurately predict TC track and intensity.

4. Conclusions

The skill of short-to-medium range weather prediction from regional or global models depends on the rate at which error builds up at the large synoptic scale from upscale cascade of errors in the small cloud scale. In order to quantify this behavior, we use a nonhydrostatic regional model and compare the intrinsic errors

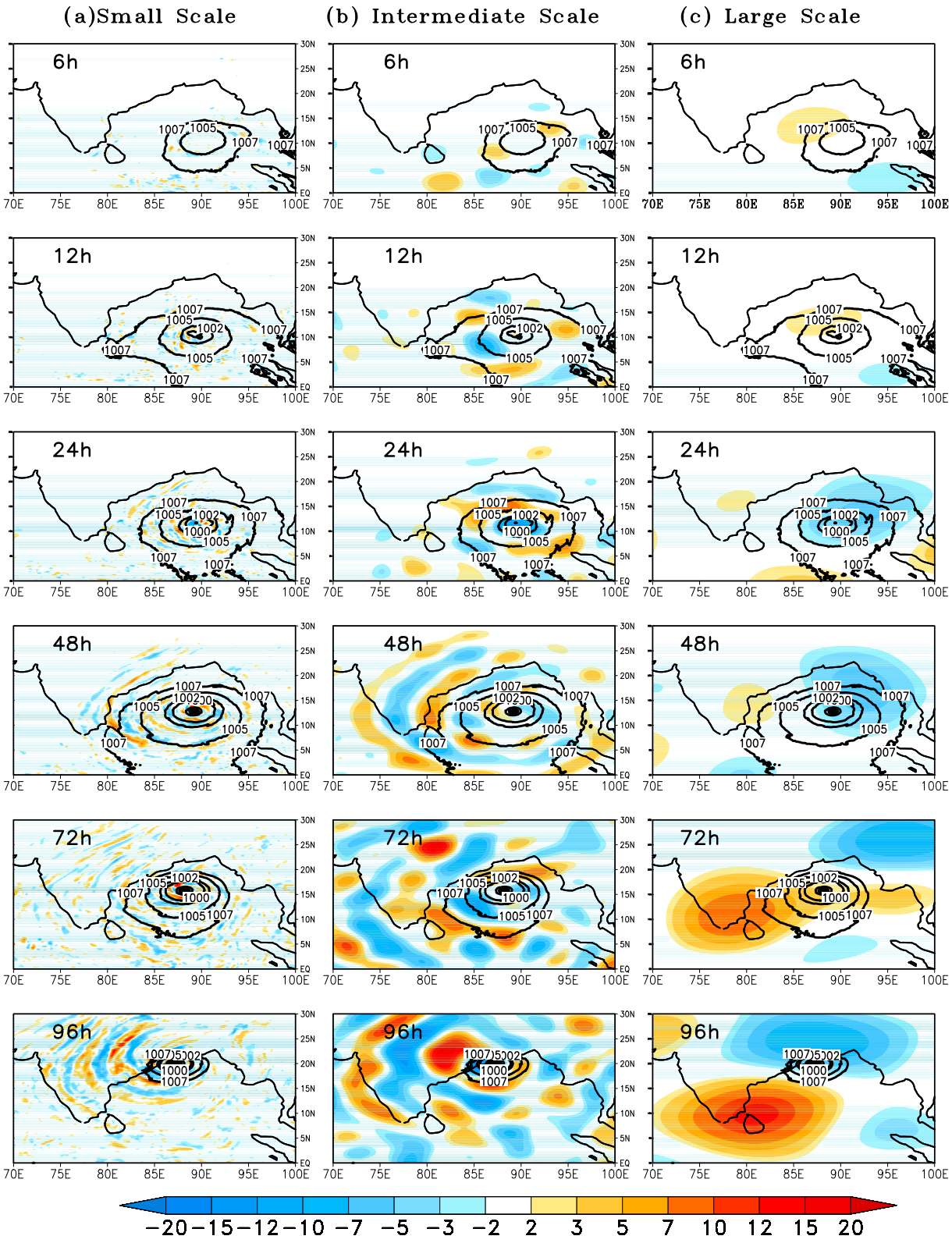

Figure 11. Time evolution of the map view of 850 hPa temperature difference (shaded) between two randomly selected ensemble members for the scales (a) less than 50 km (smaller scale), (b) between 50 and 150 km (intermediate scale), and (c) greater than 150 km (larger scale). The larger scale values are multiplied by 10, and intermediate scale values are multiplied by 2 to make all in the same color ranges. Thick contours are the sea level pressure (SLP, hPa) from the control integration that denotes the positions of the storm.

estimated by mesoscale simulations with parameterized convection at 10 km grid spacing and convection-permitting simulations at 1.1 km resolution. A series of identical twin experiments for TC cases in the Indian Ocean are designed to gain insight into the growth and primary source of errors on the larger scales.

It is demonstrated that moist convection plays a major role in intrinsic error growth that may ultimately limit the intrinsic predictability of the tropical cyclones, consistent with past studies of extratropical cyclones [*Zhang et al.,* 2002, 2003, 2007]. Error growths evolve similarly to the TC life cycle, which is expected as error growths are coupled to the moist processes, which also control the TC life cycle. More specifically, small errors in the initial conditions may grow rapidly and cascade to the larger scales through strong diabatic heating and nonlinearities associated with moist convection. Results from the numerical experiments show that model intrinsic errors start to build up from the regions of convection and ultimately affect the larger scales. It is also found that the error at small scale grows faster compared to the larger scales. The gradual increase in error energy in the large scale is a manifestation of upscale cascade of error energy from convective to large scale. This upscale spread of error would essentially limit the intrinsic predictability of the larger scales. Numerical experiments in which the latent heating from moist convection is turned off show significantly reduced error growths as they become dominantly controlled by hydrodynamic instability alone, and the development of TCs is greatly suppressed. This further supports the importance of moist processes in both error growth and TC development, so their evolutions are closely related.

By comparing simulations with parameterized and explicit convection, this study finds the convection-permitting simulations generally reproduce the observed TC tracks and intensities better than simulations that rely on convective parameterizations, particularly when the model resolution is relatively low (~30 km). However, the intrinsic predictability limit (or error growth) estimated by the 10 km simulations with parameterized convection is comparable to that estimated by convection-permitting simulations at 1.1 km resolution, both affirming the intrinsic nature of error growth in the model forecast. In other words, the cascades of errors are similar irrespective of whether moist convection is parameterized or explicitly resolved, as long as the parameterized simulations reach a spatial resolution of about 10 km. This suggests some usefulness of high-resolution (~10 km) models with parameterized convection for TC forecasting and predictability study. We note, however, that our results may be specific to the WRF model and the KF convective parameterization. In addition, systematic errors may be introduced by convective parameterizations that influence aspects of predictability not apparent from the comparison of intrinsic predictive time scales shown in our analysis. Hence, more research is needed to further compare parameterized and explicit simulations to provide more robust analysis of their relative merits in predictability study and TC forecasting.

Acknowledgments

This study is support by the Office of Science of the U.S. Department of Energy through the Regional and Global Climate Modeling Program. Pacific Northwest National Laboratory is operated for U.S. DOE by Battelle Memorial Institute under contract DE-AC06-76RLO1830. P.M., S.A., and B.N.G. acknowledge the Ministry of Earth Sciences, Government of India for supporting IITM, Pune. The authors gratefully acknowledge the suggestions and comments of Lakshmivarahan of School of Computer Science, University of Oklahoma, Norman, Oklahoma, for scientific discussions. India Meteorological Department is acknowledged for providing information about the tropical cyclone cases used in this study.

References

Bei, N., and F. Zhang (2007), Mesoscale predictability of the torrential rainfall along the Mei-yu front of China, *Q. J. R. Meteorol. Soc.*, *133*, 83–99.

Clark, A. J., W. A. Gallus Jr., M. Xue, and F. Kong (2010), Growth of spread in convection-allowing and convection-parameterizing ensembles, *Weather Forecasting*, *25*, 594–612.

Dudhia, J. (1989), Numerical study of convection observed during the winter monsoon experiment using a mesoscale two-dimensional model, *J. Atmos. Sci.*, *46*, 3077–3107.

Dudhia, J., S.-Y. Hong, and K. S. Lim (2008), A new method for representing mixed-phase particle fall speeds in bulk microphysics parameterizations, *J. Meteorol. Soc. Jpn.*, *86*, 33–44.

Elsberry, R. L., T. B. D. Lambert, and M. A. Boothe (2007), Accuracy of Atlantic and eastern North Pacific tropical cyclone intensity forecast guidance, *Weather Forecasting*, *22*, 747–762.

Emanuel, K. A. (1999), Thermodynamic control of hurricane intensity, *Nature*, *401*, 665–669.

Fang, J., and F. Zhang (2010), Initial development and genesis of Hurricane Dolly (2008), *J. Atmos. Sci.*, *67*, 655–672.

Fang, J., and F. Zhang (2011), Evolution of multi-scale vortices in the development of Hurricane Dolly (2008), *J. Atmos. Sci.*, *68*, 103–122.

Farby, F. (2006), The spatial variability of moisture in the boundary layer and its effect on convection initiation: Project-long characterization, *Mon. Weather Rev.*, *134*, 79–91.

Fuhrer, O., and C. Schär (2005), Embedded cellular convection in moist flow past topography, *J. Atmos. Sci.*, *62*, 2810–2828.

Goswami, B. N., R. S. Ajaymohan, P. K. Xavier, and D. Sengupta (2003), Clustering of low pressure systems during the Indian summer monsoon by intraseasonal oscillations, *Geophys. Res. Lett.*, *30*(8), 1431, doi:10.1029/2002GL016734.

Hendricks, E. A., M. T. Montgomery, and C. A. Davis (2004), The role of "vortical" hot towers in the formation of tropical cyclone Diana (1984), *J. Atmos. Sci.*, *61*, 1209–1232.

Hohenegger, C., and C. Schar (2007), Predictability and error growth dynamics in a cloud-resolving model, *J. Atmos. Sci.*, *64*, 4467–4478.

Hohenegger, C., D. Lüthi, and C. Schär (2006), Predictability mysteries in cloud-resolving models, *Mon. Weather Rev.*, *134*, 2095–2107.

Holland, G. J. (1997), The maximum potential intensity of tropical cyclones, *J. Atmos. Sci.*, *54*, 2519–2541.

Houze, R. A., S. S. Chen, B. F. Smull, W.-C. Lee, and M. M. Bell (2007), Hurricane intensity and eyewall replacement, *Science*, *315*, 1235–1238.

Huffman, G. J., R. F. Adler, D. T. Bolvin, G. Gu, E. J. Nelkin, K. P. Bowman, Y. Hong, E. F. Stocker, and D. B. Wolff (2007), The TRMM multi-satellite precipitation analysis: Quasi-global, multi-year, combined-sensor precipitation estimates at fine scale, *J. Hydrometeorol.*, *8*, 38–55.
Islam, S., R. L. Bras, and K. A. Emanuel (1993), Predictability of mesoscale rainfall in the tropics, *J. Appl. Meteorol.*, *32*, 297–310.
Janjic, Z. I. (1994), The step-mountain eta coordinate model: Further developments of the convection, viscous sublayer and turbulence closure schemes, *Mon. Weather Rev.*, *122*, 927–945.
Janjic, Z. I. (2002), Nonsingular Implementation of the Mellor–Yamada Level 2.5 Scheme in the NCEP Meso model, *NCEP Office Note*, *437*, 61 pp.
Kain, J. S., and J. M. Fritsch (1990), A one-dimensional entraining/detraining plume model and its application in convective parameterization, *J. Atmos. Sci.*, *47*, 2784–2802.
Kain, J. S., and J. M. Fritsch (1993), Convective parameterization for mesoscale models: The Kain-Fritcsh scheme, in *The Representation of Cumulus Convection in Numerical Models*, *Meteorol. Monogr., 46*, pp. 165–170, Am. Meteorol. Soc., Boston, Mass.
Krishnamurti, T. N., S. Pattnaik, L. Stefenova, T. S. V. Vijaykumar, B. P. Mackey, A. J. O'shay, and R. J. Pasch (2005), The hurricane intensity issue, *Mon. Weather Rev.*, *133*, 1886–1912.
Lin, J. L., et al. (2006), Tropical intraseasonal variability in 14 IPCC AR4 climate models. Part I: Convective signals, *J. Clim.*, *19*, 2665–2690.
Lin, J. L., M. I. Lee, D. Kim, I. S. Kang, and D. M. W. Frierson (2008), The impacts of convective parameterization and moisture triggering on AGCM–simulated convectively coupled equatorial waves, *J. Clim.*, *21*, 883–909.
Lin, Y., and F. Zhang (2008), Tracking mesoscale gravity waves in baroclinic jet-front systems, *J. Atmos. Sci.*, *65*, 2402–2415.
Liu, P., et al. (2009), An MJO simulated by the NICAM at 14- and 7-km resolutions, *Mon. Weather Rev.*, *137*, 3254–3268.
Madden, R. A., and P. R. Julian (1971), Detection of a 40–50 day oscillation in the zonal wind in the tropical Pacific, *J. Atmos. Sci.*, *28*, 702–708.
Madden, R. A., and P. R. Julian (1994), Observations of the 40–50-day tropical oscillation—A review, *Mon. Weather Rev.*, *122*, 814–837.
Mapes, B. E., S. Tulich, T. Nasuno, and M. Satoh (2008), Predictability aspects of global aqua-planet simulations with explicit convection, *J. Meteorol. Soc. Jpn.*, *86*, 175–185.
Martin, W. J., and M. Xue (2006), Sensitivity analysis of convection of the 24 May 2002 IHOP case using very large ensembles, *Mon. Weather Rev.*, *134*, 192–207.
Miura, H., M. Satoh, T. Nasuno, A. T. Noda, and K. Oouchi (2007), A Madden–Julian Oscillation event realistically simulated by a global cloud resolving model, *Science*, *318*, 1763–1765.
Mlawer, E. J., S. J. Taubman, P. D. Brown, M. J. Iacono, and S. A. Clough (1997), Radiative transfer for inhomogeneous atmosphere: RRTM, a validated correlated-k model for the long-wave, *J. Geophys. Res.*, *102*(D14), 16,663–16,682, doi:10.1029/97JD00237.
Monin, A. S., and A. M. Obukhov (1954), Basic laws of turbulent mixing in the surface layer of the atmosphere [in Russian], *Contrib. Geophys. Inst. Acad. Sci. USSR*, *151*, 163–187.
Mukhopadhyay, P., S. Taraphdar, and B. N. Goswami (2011), Influence of moist processes on track and intensity forecast of cyclones over the north Indian Ocean, *J. Geophys. Res.*, *116*, D05116, doi:10.1029/2010JD014700.
Oouchi, K., A. T. Noda, M. Satoh, B. Wang, S. P. Xie, H. G. Takahashi, and T. Yasunari (2009), Asian summer monsoon simulated by a global cloud-system-resolving model: Diurnal to intra-seasonal variability, *Geophys. Res. Lett.*, *36*, L11815, doi:10.1029/2009GL038271.
Pielke, R. A., Jr., J. Gratz, C. W. Landsea, D. Collins, M. Saunders, and R. Musulin (2008), Normalized hurricane damages in the United States: 1900 – 2005, *Nat. Hazards Rev.*, *9*, 29–42.
Rosenthal, S. L. (1978), Numerical simulation of tropical cyclone development with latent heat release by the resolvable scales I: Model description and preliminary results, *J. Atmos. Sci.*, *35*, 258–271.
Sato, T., H. Miura, M. Satoh, Y. N. Takayabu, and Y. Wang (2009), Diurnal cycle of precipitation in the tropics simulated in a global cloud resolving model, *J. Clim.*, *22*, 4809–4826.
Shukla, J., R. Hagedorn, B. Hoskins, J. Kinter, J. Marotzke, M. Miller, T. N. Palmer, and J. Slingo (2009), Revolution in climate prediction in both necessary and possible: A declaration at the world modelling summit for climate prediction, *Bull. Am. Meteorol. Soc.*, *90*, 175–178.
Sippel, J., and F. Zhang (2008), A probabilistic analysis of the dynamics and predictability of tropical cyclogenesis, *J. Atmos. Sci.*, *65*, 3440–3459.
Sippel, J., and F. Zhang (2010), Factors affecting the predictability of Hurricane Humberto (2007), *J. Atmos. Sci.*, *67*, 1759–1778.
Taraphdar, S., P. Mukhopadhyay, and B. N. Goswami (2010), Predictability of Indian summer monsoon weather during active and break phases using a high resolution regional model, *Geophys. Res. Lett.*, *37*, L21812, doi:10.1029/2010GL044969.
Taylor, K. E. (2001), Summarizing multiple aspects of model performance in a single diagram, *J. Geophys. Res.*, *106*, 7183–7192, doi:10.1029/2000JD900719.
Van Sang, N., R. K. Smith, and M. T. Montgomery (2008), Tropical cyclone intensification and predictability in three dimensions, *Q. J. R. Meteorol. Soc.*, *134*, 563–582.
Walser, A., and C. Schär (2004), Convection-resolving precipitation forecasting and its predictability in Alpine river catchments, *J. Hydrol.*, *288*, 57–73.
Wang, H., T. Auligne, and H. Morrison (2012), Impact of microphysics scheme complexity on the propagation of initial perturbations, *Mon. Weather Rev.*, *140*, 2287–2296.
Wang, Y. (2009), How do outer spiral rainbands affect tropical cyclone structure and intensity?, *J. Atmos. Sci.*, *66*, 1250–1273.
Wu, L., and B. Wang (2001), Effects of convective heating on movement and vertical coupling of tropical cyclones: A numerical study, *J. Atmos. Sci.*, *58*, 3639–3649.
Zhang, C. (2005), The Madden–Julian oscillation, *Rev. Geophys.*, *43*, RG2003, doi:10.1029/2004RG000158.
Zhang, F., and J. A. Sippel (2009), Effects of moist convection on hurricane predictability, *J. Atmos. Sci.*, *66*, 1944–1961.
Zhang, F., C. Snyder, and R. Rotunno (2002), Mesoscale predictability of the "surprise" snowstorm of 24–25 January 2000, *Mon. Weather Rev.*, *130*, 1617–1632.
Zhang, F., C. Snyder, and R. Rotunno (2003), Effects of moist convection on mesoscale predictability, *J. Atmos. Sci.*, *60*, 1173–1185.
Zhang, F., A. Odins, and J. W. Nielsen-Gammon (2006), Mesoscale predictability of an extreme warm-season rainfall event, *Weather Forecasting*, *21*, 149–166.
Zhang, F., N. Bei, R. Rotunno, and C. Snyder (2007), Mesoscale predictability of moist baroclinic waves: Convection permitting experiments and multistage error growth dynamics, *J. Atmos. Sci.*, *64*, 3579–3594.
Zhu, H., and A. Thorpe (2006), Predictability of extratropical cyclones: The influence of initial condition and model uncertainties, *J. Atmos. Sci.*, *63*, 1483–1497.